Digital Quantum Simulation of the Schwinger Model and Symmetry Protection with Trapped Ions

Nhung H. Nguyen,[1,*] Minh C. Tran,[2,3] Yingyue Zhu,[1] Alaina M. Green,[1] C. Huerta Alderete,[1] Zohreh Davoudi,[4] and Norbert M. Linke[1,5]

[1] *Joint Quantum Institute and Department of Physics, University of Maryland, College Park, Maryland 20742, USA*

[2] *Center for Theoretical Physics, Massachusetts Institute of Technology, Cambridge, Massachusetts 02139, USA*

[3] *Department of Physics, Harvard University, Cambridge, Massachusetts 02138, USA*

[4] *Maryland Center for Fundamental Physics and Department of Physics, University of Maryland, College Park, Maryland 20742, USA*

[5] *Duke Quantum Center and Department of Physics, Duke University, Durham, North Carolina 27708, USA*

(Received 7 January 2022; accepted 21 March 2022; published 4 May 2022)

Tracking the dynamics of physical systems in real time is a prime application of quantum computers. Using a trapped-ion system with up to six qubits, we simulate the real-time dynamics of a lattice gauge theory in $1+1$ dimensions, i.e., the lattice Schwinger model, and demonstrate nonperturbative effects such as pair creation for times much longer than previously accessible. We study the gate requirement of two formulations of the model using the Suzuki-Trotter product formula, as well as the trade-off between errors from the ordering of the Hamiltonian terms, the Trotter step size, and experimental imperfections. To mitigate experimental errors, a recent symmetry-protection protocol for suppressing coherent errors and a symmetry-inspired postselection scheme are applied. This work demonstrates the integrated theoretical, algorithmic, and experimental approach that is essential for efficient simulation of lattice gauge theories and other complex physical systems.

DOI: 10.1103/PRXQuantum.3.020324

I. INTRODUCTION

An exciting prospect for quantum computers is the simulation of complex physical systems [1,2]. Digital quantum computers can simulate a wide range of physical Hamiltonians, since one can often find efficient circuit decompositions to approximate their dynamics. However, the number of qubits and the achievable circuit depth in experiments are limited. In particular, it is challenging to simulate larger systems for longer times while maintaining the fidelity of the simulations. To address this challenge, there has been substantial theoretical research on finding optimal simulation algorithms with improved theoretical error bounds [3–10] and better empirical performance [11,12], as well as efficient circuit decomposition with resource analysis for a range of problems [12–28]. Furthermore, symmetry-protection schemes have emerged to suppress algorithmic and experimental errors [29–36], along with noise-mitigation schemes for extrapolating to the noiseless limit of observables [37–45]. As a result, it is of great interest to study how well these recent algorithmic advances, which mostly concern asymptotic regimes with a large number of qubits and long evolution times, apply in a current experiment.

The physical system we consider is a low-dimensional lattice gauge theory. Gauge field theories are the underlying formalism describing interactions among elementary particles in the Standard Model and are prime candidates for modeling physics beyond the Standard Model. They further provide a powerful theoretical framework for describing low-energy excitations in condensed-matter systems. There has been tremendous progress in applying nonperturbative methods to solve lattice gauge theories in various systems and coupling regimes [46–51]. However, evaluation of the real-time dynamics of gauge field theories remains challenging in the strong-coupling regime, where a notorious sign problem halts Monte Carlo based classical simulations [52]. Both fermionic and bosonic degrees of freedom in gauge theories, when defined on a discretized spacetime, can be mapped to spins and, in principle, efficiently simulated using quantum

*nhunghng@umd.edu

simulators. A simple Abelian low-dimensional gauge theory is quantum electrodynamics in $1+1$ dimensions, or the Schwinger model [53]. It exhibits nontrivial dynamics similar to those seen in quantum chromodynamics in $3+1$ dimensions, i.e., the theory of the strong force in nature, including particle-antiparticle pair creation, chiral symmetry breaking, confinement, and a nontrivial θ-vacuum [54,55]. The Hamiltonian formulation of the lattice Schwinger model, i.e., the Schwinger model defined in a discretized space and with continuous time, has served as a test bed for numerous computational techniques in recent years, including quantum simulation and computation. In particular, there have been several theoretical proposals for analog quantum simulation [56–62] and gate-based quantum algorithms [22,24,63–70] of the Schwinger model, along with experimental implementations on various quantum platforms such as trapped ions [71,72], Rydberg atoms [60,73], ultracold atoms [74,75], and superconducting qubits [64,76].

Inspired by the first digital simulation of the Schwinger model in Ref. [71], we revisit the simulation to answer the following questions. (i) Are larger and longer simulations of lattice gauge theories viable on present hardware? (ii) Given recent progress in quantifying the theoretical and empirical bounds on simulation algorithms, what are the resource requirements of simulating the lattice Schwinger model in the purely fermionic formulation with long-range interactions versus the fermion-boson formulation with only local interactions? (iii) What are the theoretical considerations in decomposing the time-evolution operator using product formulas, e.g., how does the Trotter error depend on the ordering of terms in each Trotter step of the evolution, what order of the product formula should one use, and how small should the Trotter steps be, considering the anticipated size of the experimental error? (iv) Can recent cost-efficient symmetry protection protocols provide insights into the nature of experimental errors?

To address these questions, we realize experimentally the time dynamics of the lattice Schwinger model in its staggered formulation [77] and within its purely fermionic representation, for two-, four-, and six-site theories. Along with the experimental demonstration, different term orderings and product formulas are studied and the gate complexity of the algorithm used here is compared with another algorithm in the local formulation of the same theory [22]. The symmetry protection of Ref. [29] is implemented for the first time in experiment, in addition to a simple symmetry-inspired postselection.

II. THEORY AND ALGORITHM CONSIDERATIONS

In the staggered formulation of the lattice Schwinger model introduced by Kogut and Susskind (KS) [77], the two-component matter field at one spatial site is split into two one-component fields, $\hat{\psi}$, each occupying one site of the staggered lattice. This staggering corresponds to placing electrons at odd sites and positrons at even sites. The electric field, $\hat{E}$, and the corresponding gauge-link variable, $\hat{U}$, are defined on the link connecting the two adjacent staggered sites. The Hamiltonian in natural units is

$$\hat{H}_{\mathrm{KS}} = \frac{i}{2a}\sum_{n=1}^{N-1}(\hat{\psi}_n^\dagger \hat{U}_n \hat{\psi}_{n+1} - \mathrm{H.c.}) + \frac{g^2 a}{2}\sum_{n=1}^{N-1}\hat{E}_n^2 + \frac{m}{2}\sum_{n=1}^{N}(-1)^n \hat{\psi}_n^\dagger \hat{\psi}_n, \tag{1}$$

where N is the number of staggered sites, m is the mass of the fermions, a denotes the lattice spacing, and g is the coupling constant. The first term in the Hamiltonian involves gauge-boson-assisted fermionic hopping between nearest-neighbor sites. The second term is the energy stored in the electric field. The last term represents the rest mass of the fermions in the staggered formulation. The theory exhibits a local gauge symmetry, which leads to a Gauss's law constraint on the allowed physical states $|\phi\rangle_{\mathrm{phys}}$. This constraint enforces the net electric field at each site to be balanced by the electric charge present at the site, i.e., $\hat{G}_n|\phi\rangle_{\mathrm{phys}} = 0$ with $\hat{G}_n = \hat{E}_n - \hat{E}_{n-1} - \hat{\psi}_n^\dagger\hat{\psi}_n + \frac{1}{2}[1-(-1)^n]$ for all n.

The matter-field operators in Eq. (1) can be mapped to spin operators by the Jordan-Wigner transformation: $\hat{\psi}_n = \prod_{l<n}(i\hat{\sigma}_l^Z)\hat{\sigma}_n^-$ and $\hat{\psi}_n^\dagger = \prod_{l<n}(-i\hat{\sigma}_l^Z)\hat{\sigma}_n^+$, with $\hat{\sigma}_n^\pm = \frac{1}{2}(\hat{\sigma}_n^X \pm i\hat{\sigma}_n^Y)$. With open boundary conditions (OBCs), the gauge links and the electric fields can be eliminated upon a gauge transformation and the application of Gauss's law [78]. Without loss of generality, the electric field coming into the lattice is set to zero, and the resulting spin Hamiltonian reads

$$\begin{aligned}\hat{H} &= x\sum_{n=1}^{N-1}(\hat{\sigma}_n^X\hat{\sigma}_{n+1}^X + \hat{\sigma}_n^Y\hat{\sigma}_{n+1}^Y) \\ &\quad + \frac{1}{4}\sum_{n=1}^{N-1}\left[\sum_{m=1}^{n}\left(\hat{\sigma}_m^Z + (-1)^m\right)\right]^2 + \mu\sum_{n=1}^{N}(-1)^n\frac{\hat{\sigma}_n^Z+1}{2} \\ &\equiv \hat{H}^x + \hat{H}^{ZZ} + \hat{H}^Z + \mathrm{const.}\end{aligned} \tag{2}$$

Here, the original Hamiltonian is rescaled by $\frac{2}{ag^2}$, i.e., $\hat{H} = \frac{2}{ag^2}\hat{H}_{\mathrm{KS}}$, so that $\hat{H}$ in Eq. (2) is dimensionless with parameters $x = \frac{1}{g^2a^2}$ and $\mu = \frac{2m}{ag^2}$. $\hat{H}^x$ denotes the term proportional to the coupling x, $\hat{H}^{ZZ}$ consists of (nearly) all-to-all spin-spin interactions proportional to $\hat{\sigma}_n^Z\hat{\sigma}_m^Z$, and $\hat{H}^Z$ is the sum of the terms proportional to $\hat{\sigma}_n^Z$. The constant terms are ignored in the following as they do not affect the evolution. By convention, $\hat{\sigma}^Z|0\rangle = |0\rangle, \hat{\sigma}^Z|1\rangle = -|1\rangle$, and the

presence of a particle (antiparticle) is encoded as $|1\rangle$ ($|0\rangle$) at an odd (even) site. Therefore, for an N-site system, the bare-vacuum state, i.e., the ground state of the theory in the $x = 0$ limit, is $|\psi_0\rangle \equiv (|01\rangle)^{\otimes N/2}$.

The goal is to study the real-time dynamics of bare-vacuum fluctuations and particle-antiparticle pair creation. One can therefore perform a quench experiment where the simulation is initiated in the bare-vacuum state, $|\psi(0)\rangle = |\psi_0\rangle$, which is then evolved via the Hamiltonian in Eq. (2) with $x \neq 0$. The survival probability of the bare-vacuum state is

$$P_{\text{vac}}(t) = |\langle\psi(0)|\psi(t)\rangle|^2 = \left|\langle\psi(0)|\, e^{-it\hat{H}}\, |\psi(0)\rangle\right|^2 \quad (3)$$

and the particle-number density is $\nu(t) = \frac{1}{N}\sum_{n=1}^{N} \nu_n(t)$ with

$$\nu_n(t) = \langle\psi(t)|\frac{(-1)^n\hat{\sigma}_n^Z + 1}{2}|\psi(t)\rangle\,. \quad (4)$$

In the limit of $N \to \infty$, the two quantities are related to each other via $\nu(t) = -\frac{1}{N}\log(P_{\text{vac}})$ [53]. The local charge density is defined as

$$Q_n(t) \equiv \langle\psi(t)|\frac{\hat{\sigma}_n^Z + (-1)^n}{2}|\psi(t)\rangle \quad (5)$$

$$= \langle\psi(t)|\hat{E}_n - \hat{E}_{n-1}|\psi(t)\rangle\,, \quad (6)$$

where the charge of the particle (antiparticle) is -1 (1). The local charge density is related to the local particle-number density by $Q_n(t) = (-1)^n\nu_n(t)$. As there is no interaction in the Hamiltonian that changes the total net charge of the system, $\sum_n Q_n$ is conserved. Therefore, the model has a global symmetry operator $\hat{S}_z = \sum_n \hat{\sigma}_n^Z$, which is consistent with the symmetry of an XXZ Heisenberg spin Hamiltonian.

To perform the unitary evolution $\hat{\mathcal{U}}(t) = e^{-it\hat{H}}$ with $\hat{H} \equiv \sum_{k=1}^{K}\hat{h}_k$ on a quantum computer, with noncommuting Hamiltonian terms $\hat{h}_k$, the evolution can be broken into r smaller time steps of size $\delta t = t/r$. For each time step, the unitary $\hat{\mathcal{U}}(\delta t)$ is approximated by a product formula, which can then be implemented in terms of the available native gates. For the first-order product formula,

$$\hat{\mathcal{S}}_1(\delta t) = \prod_{k=1}^{K} e^{-i\delta t\hat{h}_k}, \quad (7)$$

while for the second-order product formula,

$$\hat{\mathcal{S}}_2(\delta t) = \prod_{k=1}^{K} e^{-i\frac{\delta t}{2}\hat{h}_k}\prod_{k=K}^{1} e^{-i\frac{\delta t}{2}\hat{h}_k}, \quad (8)$$

where the second product is realized in reversed order. Higher-order formulas $\hat{\mathcal{S}}_p(\delta t)$ can also be constructed recursively for even integers p [79].

While it is generally difficult to obtain an exact estimate for the Trotter error in the pth-order product formula, progress in recent years has resulted in tighter error bounds for them. For example, a nearly optimal bound is derived in Ref. [3], expressed in terms of the nested commutators between different $\hat{h}_k$ terms. For the error of the second-order formula,

$$\begin{aligned}\left\|\hat{\mathcal{U}}(\delta t) - \hat{\mathcal{S}}_2(\delta t)\right\| &\leq \frac{(\delta t)^3}{24}\sum_{k_1=1}^{K-1}\left\|\left[\hat{h}_{k_1},\left[\hat{h}_{k_1},\sum_{k_2=k_1+1}^{K}\hat{h}_{k_2}\right]\right]\right\| \\ &+ \frac{(\delta t)^3}{12}\sum_{k_1=1}^{K-1}\left\|\left[\sum_{k_3=k_1+1}^{K}\hat{h}_{k_3},\left[\sum_{k_2=k_1+1}^{K}\hat{h}_{k_2},\hat{h}_{k_1}\right]\right]\right\|.\end{aligned} \quad (9)$$

The norms of nonvanishing nested commutators can be further upper bounded using the triangle inequality $\|[A,B]\| \leq 2\,\|A\|\,\|B\|$, resulting in closed-form, albeit looser, error bounds. Based on this approach, an upper bound for the pth-order formulas in simulating a two-body Hamiltonian can be obtained:

$$\left\|\hat{\mathcal{U}}(\delta t) - \hat{\mathcal{S}}_p(\delta t)\right\| \leq \kappa_p\gamma\lambda^p(\delta t)^{p+1}, \quad (10)$$

where $\kappa_p = (4\times 5^{p/2-1})^{p+1}p!/2$ is a constant, λ is the maximum strength of the sum of the interactions that involve any particular site, and $\gamma = \sum_{k=1}^{K-1}\|\hat{h}_k\|$. Since γ only involves the first $K-1$ terms of the Hamiltonian, labeling the index k such that $\hat{h}_K$ is the term with the largest norm typically results in the smallest error bound.

Given a small δt, a higher-order formula results in a smaller simulation error. However, since the gate count of $\hat{\mathcal{S}}_p(\delta t)$ scales as $\mathcal{O}\left(5^{p/2}\right)$, increasing p increases the gate complexity of the simulation exponentially. The optimal choice for p is a balance between the gate depth, the evolution time t, and the error tolerance of the simulation. Since the experimental error can dominate the Trotter error at long evolution times, the first-order product formula, which minimizes the gate count per Trotter step, turns out to be a more suitable choice for the experiment in this work.

A. Term ordering

Generally, the Hamiltonian terms in Eq. (2) do not commute. Therefore, one needs to find the optimal ordering in the application of the product formula to minimize the Trotter error. There are two typical orderings of the

terms in a nearest-neighbor Heisenberg spin model. The odd-even ordering is defined as having the odd-leading two-spin terms, e.g., $\hat{\sigma}^{\tau}_{2k-1}\hat{\sigma}^{\tau}_{2k}$ with $\tau = X, Y, Z$ and $1 \leq k \in \mathbb{Z}$, applied first, then applying the even-leading two-spin terms, e.g., $\hat{\sigma}^{\tau}_{2k}\hat{\sigma}^{\tau}_{2k+1}$, followed by the single-body terms (if any). In the XYZ ordering, the terms involving $\hat{\sigma}^X$ are applied first, followed by the terms involving $\hat{\sigma}^Y$, and finally those involving $\hat{\sigma}^Z$. It is known that the odd-even ordering introduces less Trotter error than the XYZ ordering [11]. Here, we investigate whether the odd-even ordering is also a better choice for simulating the Schwinger model, which includes both nearest-neighbor and (nearly) all-to-all spin-spin interactions.

Since $\hat{H}^x$ in the Hamiltonian in Eq. (2) includes only nearest-neighbor interactions, one way to define an odd-even-ordered product formula is to apply the odd-even ordering to terms in $\hat{H}^x$ only. If we define $\hat{H}^x_{n,m}$ to be the term in $\hat{H}^x$ acting on sites n and m and, similarly, $\hat{H}^{ZZ}_{n,m}$ to be the term in $\hat{H}^{ZZ}$ acting on sites n and m, this ordering can be written as

$$\hat{\mathcal{S}}_1^{\mathrm{oe1}}(\delta t) = e^{-i\delta t \hat{H}^Z} e^{-i\delta t \hat{H}^{ZZ}} \times \prod_{k=1}^{(N/2)-1} e^{-i\delta t \hat{H}^x_{2k,2k+1}} \prod_{k=1}^{N/2} e^{-i\delta t \hat{H}^x_{2k-1,2k}}. \quad (11)$$

Alternatively, the odd-even ordering can be applied to both $\hat{H}^x$ and the nearest-neighbor terms in $\hat{H}^{ZZ}$, followed by the application of the non-nearest neighbor terms in $\hat{H}^{ZZ}$ as well as $\hat{H}^Z$:

$$\hat{\mathcal{S}}_1^{\mathrm{oe2}}(\delta t) = e^{-i\delta t \hat{H}^Z} \prod_{n=1}^{N-1} \prod_{m=1}^{n-2} e^{-i\delta t \hat{H}^{ZZ}_{m,n}} \times \prod_{k=1}^{(N/2)-1} e^{-i\delta t \hat{H}^{ZZ}_{2k,2k+1}} e^{-i\delta t \hat{H}^x_{2k,2k+1}} \times \prod_{k=1}^{N/2} e^{-i\delta t \hat{H}^{ZZ}_{2k-1,2k}} e^{-i\delta t \hat{H}^x_{2k-1,2k}}. \quad (12)$$

The two odd-even-ordered evolution operators are related by a rotation around the Z axis:

$$\hat{\mathcal{S}}_1^{\mathrm{oe1}} = \left(\prod_{k=1}^{N/2} e^{-i\delta t \hat{H}^{ZZ}_{2k-1,2k}}\right) \hat{\mathcal{S}}_1^{\mathrm{oe2}} \left(\prod_{k=1}^{N/2} e^{i\delta t \hat{H}^{ZZ}_{2k-1,2k}}\right). \quad (13)$$

As a result, if the state is initialized and measured in the Z basis, one arrives at the same measurement outcome using either scheme. Therefore, in the following we only consider $\hat{\mathcal{S}}_1^{\mathrm{oe1}}$ because it requires the implementation of fewer single-qubit gates.

The symmetry operator $\hat{S}_z$ commutes with $\hat{\sigma}^X_n\hat{\sigma}^X_{n+1} + \hat{\sigma}^Y_n\hat{\sigma}^Y_{n+1} = \hat{\sigma}^+_n\hat{\sigma}^-_{n+1} + \mathrm{H.c.}$, which is not broken up by the odd-even ordering scheme. Therefore, this ordering does not result in any leakage to the symmetry-forbidden subspace. This is unlike the XYZ ordering that implements

$$\hat{\mathcal{S}}_1^{\mathrm{XYZ}}(\delta t) = e^{-i\delta t \hat{H}^Z} e^{-i\delta t \hat{H}^{ZZ}} \times \prod_{k=1}^{N-1} e^{-i\delta t \hat{H}^{(YY)}_{k,k+1}} \prod_{k=1}^{N-1} e^{-i\delta t \hat{H}^{(XX)}_{k,k+1}}, \quad (14)$$

where $\hat{H}^{(XX)}_{k,k+1}$ and $\hat{H}^{(YY)}_{k,k+1}$ are the terms in the Hamiltonian in Eq. (2) proportional to $\hat{\sigma}^X_k\hat{\sigma}^X_{k+1}$ and $\hat{\sigma}^Y_k\hat{\sigma}^Y_{k+1}$, respectively. The size of the leakage to the symmetry-forbidden subspace for both schemes is verified numerically in Fig. 1.

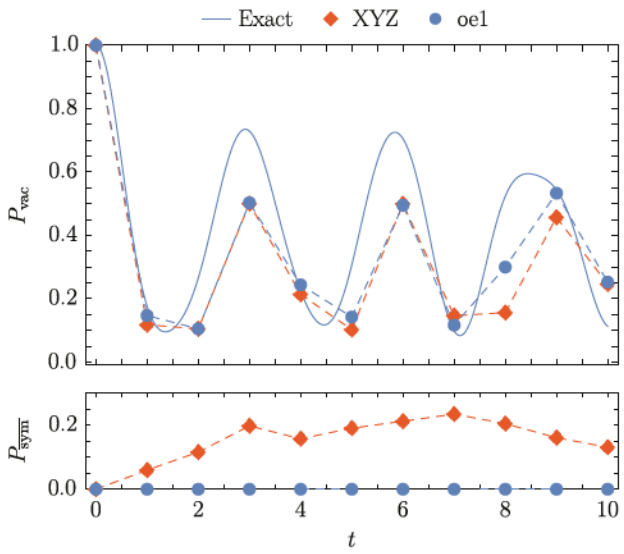

FIG. 1. The numerical simulation of the projection on the bare-vacuum state P_{vac} (upper panel) and the population of symmetry-forbidden states $P_{\overline{\mathrm{sym}}}$ (lower panel) when the system is initialized in the bare-vacuum state for $N = 6$, $\mu = 0.1$, and $x = 0.6$. Different term orderings for the Trotterized evolution are considered: the odd-even ordering defined in Eq. (11) (blue dots) and the XYZ ordering defined in Eq. (14) (red diamonds). The blue line denotes the exact evolution.

B. Gate complexity

There are different approaches to digitally simulating the Schwinger model. Reference [22] truncates the gauge-boson degrees of freedom in the electric field basis, $|E| \leq \Lambda$. The electric field Hilbert space at each link is then encoded using $\log_2(2\Lambda + 1)$ qubits. With OBCs and a zero incoming electric field flux, the exact theory is recovered for $\Lambda = N/2$. To simulate the model with N sites for time t, this approach requires $\mathcal{O}(N + N\log_2 N)$ qubits and, up to logarithmic corrections, $\mathcal{O}\left(N^{5/2}t^{3/2}\right)$ two-qubit gates, using the second-order Suzuki-Trotter formula. In contrast, our approach integrates out the gauge bosons, leaving only the fermionic degree of freedom associated with the

matter fields [71,78]. Therefore, it requires $\mathcal{O}(N \log_2 N)$ fewer qubits to simulate the same model. However, in this approach, one trades the local gauge-matter interactions for long-range matter-matter interactions that correspond to a Coulomb force. Here, we investigate whether this purely fermionic model increases the gate complexity of the simulation compared with the local formulation involving both fermions and bosons.

Given a fixed error tolerance, one can use Eq. (10) to estimate the required number of Trotter steps in the purely fermionic formulation for simulation time t, system size N, and at fixed x and μ:

$$\mathcal{O}\left(\lambda\gamma^{1/p}t^{1+1/p}\right) = \mathcal{O}\left(N^{2+1/p}t^{1+1/p}\right). \tag{15}$$

Here, $\lambda = \mathcal{O}\left(N^2\right)$, which is determined by the interactions in $\hat{H}^{ZZ}$, and $\gamma = \mathcal{O}\left(N\right)$, which results from summing over only the interactions in $\hat{H}^{x}$ [80]. Since each Trotter step requires $\mathcal{O}\left(N^2\right)$ two-qubit gates, the gate complexity of the pth-order product formula is $\mathcal{O}\left(N^{4+1/p}t^{1+1/p}\right)$. For the second-order product formula ($p = 2$), the gate complexity reduces to $N^{9/2}t^{3/2}$, which is a factor of N^2 larger than the scaling of Ref. [22].

The bound on the Trotter error derived above is an upper bound and the required gate count may be much smaller in practice. In Fig. 2, we plot the empirical value of the number of two-qubit gates required for simulating the time-evolution operator in the purely fermionic formulation using the second-order formula for time $t = N$. The empirical gate count is obtained through a binary search for the minimum number of Trotter steps such that the difference between the Trotterized and the exact evolution is at most $\epsilon = 0.01$. This value is compared to two bounds: the commutator bound obtained from Eq. (10), following the discussion above, and the exact commutator bound derived from computing the norms of the nested commutators in Eq. (9) exactly. The gate complexity $\mathcal{O}\left(N^{6.2}\right)$ from the commutator bound agrees with our earlier estimate of $\mathcal{O}\left(N^6\right)$ for this formulation of the model. However, Fig. 2 shows that this bound, obtained by applying the triangle inequality on the norms of the nested commutators, is rather loose. Instead, by computing Eq. (9) exactly, hence invoking cancellations between the commutators, the gate complexity reduces to $\mathcal{O}\left(N^{4.6}\right)$, very close to the empirical scaling of $\mathcal{O}\left(N^{4.2}\right)$. Notably, the empirical scaling is nearly the same as the scaling of Ref. [22] for the fermion-boson formulation. However, we note that one may also be able to obtain tighter error bounds on the algorithm of Ref. [22] empirically.

C. Symmetry protection

The digitization of a quantum evolution may introduce errors that populate states forbidden by the symmetry of the target system. Reference [29] proposes a method to reduce this leakage when using product formulas and applies it to the fermion-boson formulation of the Schwinger model. In this section, we discuss whether the proposed method is effective at protecting the symmetry of the purely fermionic formulation and in reducing the Trotter error.

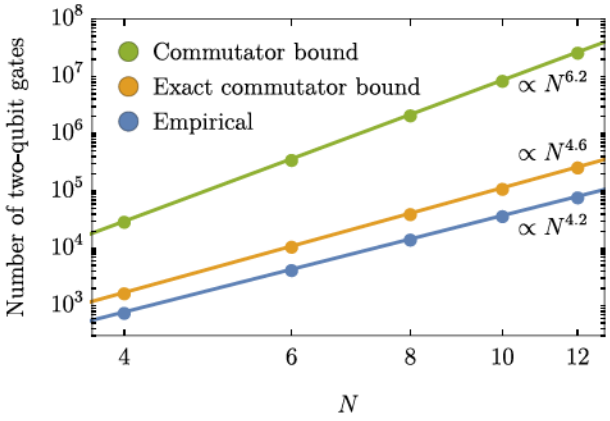

FIG. 2. The number of two-qubit gates required to simulate the time evolution under the Hamiltonian in Eq. (2) on an N-site lattice for time $t = N$ given an error tolerance $\epsilon = 0.01$, and using the second-order product formula in Eq. (8). The commutator bound on the gate complexity (green dots) is estimated from the error bound in Eq. (10). We also obtain a tighter estimate (orange dots) by exactly computing the nested commutators in Eq. (9). Finally, the empirical gate count (blue dots) is obtained through a binary search for the minimum number of time steps $t/\delta t$ such that the total error is at most ϵ. The straight lines are linear fits that result in the polynomial scaling given in the figure.

As mentioned earlier, the Schwinger-model Hamiltonian in Eq. (2) is invariant under a global rotation around the Z axis of the qubits, i.e., $[\hat{H}, \hat{S}_z] = 0$. Therefore, the expectation value of $\hat{S}_z$ is conserved if the evolution is exact. However, due to Trotterization errors, $\langle\hat{S}_z\rangle$ may deviate from its initial value during the simulation. To mitigate this error, one can insert rotations generated by the symmetry, i.e., $\hat{C}(\alpha) = e^{-i\alpha\hat{S}_z}$, in between the Trotter steps [29]:

$$\hat{\mathcal{U}}(t) = \prod_{k=1}^{t/\delta t}\hat{\mathcal{U}}_k(\delta t) \longrightarrow \prod_{k=1}^{t/\delta t}\hat{C}^\dagger(\alpha_k)\hat{\mathcal{U}}_k(\delta t)\hat{C}(\alpha_k). \tag{16}$$

By choosing suitable angles α_k for different Trotter steps, the errors from each step that do not commute with $\hat{S}_z$ are rotated by different amounts and can interfere destructively. This results in smaller leakage to the sector with the global charges that differ from the initial state. Therefore, the method mitigates errors in symmetry-violating Trotterization schemes, such as the XYZ ordering. Errors that commute with $\hat{S}_z$ remain intact under these rotations $\hat{C}(\alpha_k)$. As the result, this method has no effect on symmetry-preserving Trotterization schemes, such as the odd-even

ordering. Additionally, since the symmetry operator $\hat{S}_z$ is diagonal in the measurement basis for the observables considered here, one can simply mitigate symmetry-violating errors by postselecting on measurement outcomes that preserve $\langle \hat{S}_z \rangle$. We compare the two mitigation methods in the following.

For simplicity, the angles α_k in Eq. (16) can be chosen such that $\alpha_k = k\alpha_1$, where, for each t, α_1 is determined by numerically minimizing the leakage to the symmetry-forbidden subspace after $t/\delta t$ steps, as detailed in Appendix A. As a result, the optimal value of α_1 depends on the number of Trotter steps and the simulation time. The top panel in Fig. 3 plots the leakage to the symmetry-forbidden sector for the odd-even ordering and the XYZ ordering before and after postselection, as well as the XYZ ordering with symmetry protection but without postselection. As expected, the odd-even ordering results in no population in the symmetry-forbidden states and the leakage seen in the XYZ ordering trivially goes to zero after postselection. Importantly, the symmetry-protected XYZ ordering leads to a strong suppression of the leakage.

However, this improvement in preserving the symmetry does not guarantee a smaller Trotter error. Given two operators $\mathcal{E}_{\text{sym}}$ and $\mathcal{E}_{\overline{\text{sym}}}$, corresponding to the symmetry-preserving and symmetry-violating errors in the simulation, respectively, it is generally not true that $\|\mathcal{E}_{\text{sym}}\| < \|\mathcal{E}_{\text{sym}} + \mathcal{E}_{\overline{\text{sym}}}\|$. In particular, depending on the observable of interest, the effect of the two types of errors may interfere destructively. Therefore, elimination of $\mathcal{E}_{\overline{\text{sym}}}$ may actually increase the error in the expectation value of the observable. For example, as shown in the lower panel of Fig. 3, the symmetry protection sometimes increases the error in the population of the bare-vacuum state instead of decreasing it. Overall, symmetry protection does not improve the accuracy of the XYZ ordering scheme over the odd-even ordering scheme. Notably, postselection is more successful than the symmetry-protection scheme at mitigating the Trotter error in P_{vac}.

According to Ref. [29], the symmetry protection scheme mitigates time-correlated experimental errors as well. Since the errors in our experiment are expected to be

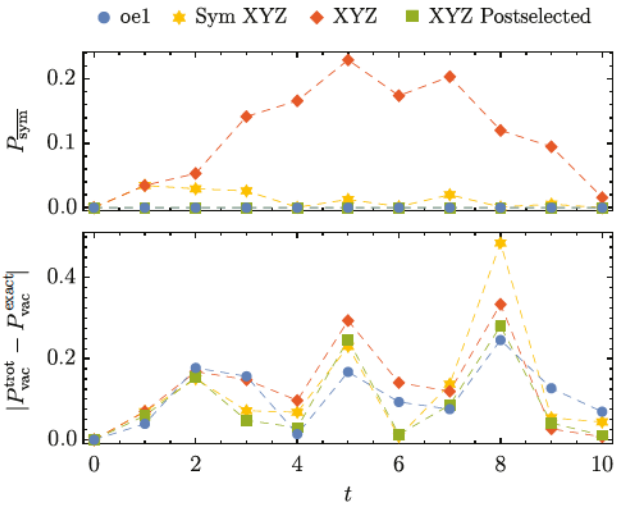

FIG. 3. The leakage to the symmetry-forbidden sector, $P_{\overline{\text{sym}}}$, defined as the population in the states with a nonvanishing total charge given a bare-vacuum initial state (upper panel), as well as the error in the bare-vacuum population (lower panel) are shown for the odd-even ordering (blue dots), the XYZ ordering before (red diamonds) and after (green squares) postselection, as well as the XYZ ordering with symmetry protection but without postselection (yellow stars). The parameters used for the plot are $\mu = 0.1$, $x = 0.6$, $N = 4$, and $\delta t = 1$. The optimal angles for the symmetry-protected simulation are provided in Appendix A. Sym XYZ refers to symmetry-protected XYZ ordering.

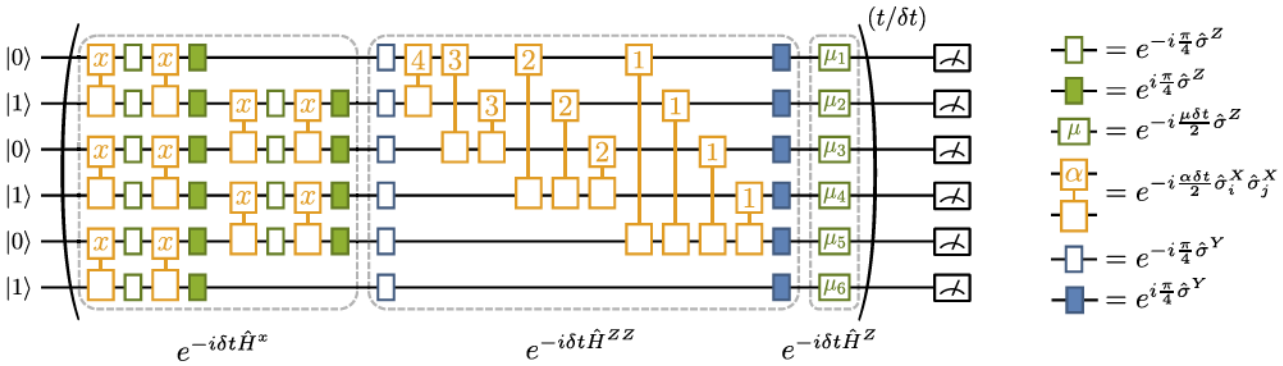

FIG. 4. The circuit for the Trotterized evolution according to the Hamiltonian in Eq. (2) for $N = 6$ lattice sites, with odd-even ordering of the Trotter decomposition introduced in Eq. (11). The interaction term $e^{-i\delta t\hat{H}^x}$ is implemented with nearest-neighbor X_iX_{i+1} and Y_iY_{i+1} gates. The $e^{-i\delta t\hat{H}^{ZZ}}$ term is implemented with X_iX_j and R_i rotations. The $e^{-i\delta t\hat{H}^Z}$ term involves only Z_i rotations, with the angles $\mu_1 = -(\mu+3)\delta t$, $\mu_2 = (\mu-2)\delta t$, $\mu_3 = -(\mu+2)\delta t$, $\mu_4 = (\mu-1)\delta t$, $\mu_5 = -(\mu+1)\delta t$, and $\mu_6 = \mu\delta t$. Qubits are initialized in the bare-vacuum state $|010101\rangle$, then evolved by repeating the circuit in the parentheses $t/\delta t$ times, and measured individually in the Z basis at the end.

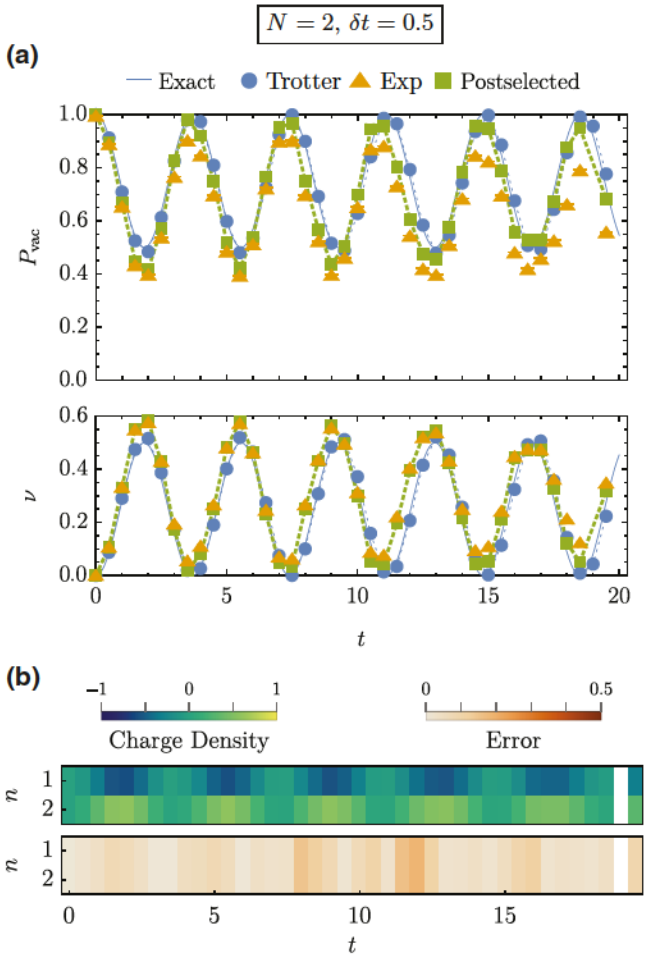

FIG. 5. Experimental results for $N = 2$ and $\delta t = 0.5$. (a) The upper plot shows fluctuation in the bare-vacuum population, P_{vac}, while the lower plot shows the particle-number density, ν, as a function of time, indicating the creation and annihilation of the particle-antiparticle pairs. The dashed lines are a guide to the eye. (b) The upper plot shows the local charge density Q_n as measured in the experiment after postselection, while the lower plot shows its deviation from theory as a function of time.

dominated by uncorrelated noise, it is interesting to investigate how well the scheme performs in the experimental implementation. To isolate the effects of symmetry protection on experimental rather than Trotter errors, we implement the odd-even ordering, which preserves the symmetry. The results are presented at the end of Sec. III.

III. EXPERIMENT AND RESULTS

The experiment consists of a chain of up to nine $^{171}\text{Yb}^+$ ions held in a linear Paul trap, with up to six ions used as qubits. The two qubit states are realized in the hyperfine-split ground level, $|0\rangle = |^2S_{1/2}\, F = 0, m_F = 0\rangle$ and $|1\rangle = |^2S_{1/2}\, F = 1, m_F = 0\rangle$. The qubits are initialized to $|0\rangle$ by optical pumping, and read out on a multichannel photodetector using state-dependent fluorescence [81]. We use two counterpropagating Raman beams to coherently manipulate the states of the qubits [82]. One Raman beam is split into individual beams to address each qubit separately. The native gates in this setup are single-qubit Z rotations, $Z_i(\theta) = e^{-i\theta/2\,\hat{\sigma}_i^Z}$, single-qubit rotations around the equatorial plane of the Bloch sphere $R_i(\theta,\phi) = e^{-i\theta/2\,(\hat{\sigma}_i^X\cos\phi+\hat{\sigma}_i^Y\sin\phi)}$, and two-qubit gates $X_iX_j(\chi) = e^{-i\chi\hat{\sigma}_i^X\hat{\sigma}_j^X}$, where ϕ is the angle of the axis of rotation and θ and χ are the rotation angles. The Z rotations are implemented as classical phase advances and therefore are practically noise free. The single-qubit gates $R_i(\theta,\phi)$ are realized by driving a qubit on resonance, with the laser phase set to ϕ and the duration proportional to θ. The two-qubit gates use the shared motional modes of the ion chain to mediate interactions between pairs of ions [83–85]. Carefully designed amplitude modulation of the laser pulse leaves the qubit states decoupled from the motion at the end of the gate [86]. The individual addressing beams allow any pair of ions to be entangled, making the system a fully connected programmable quantum computer. More details on the setup and gate fidelity are presented in Ref. [82,87,88].

TABLE I. Gate counts for simulating each Trotter step of the time evolution in the Schwinger model with the odd-even term ordering in Eq. (11), along with the largest number of Trotter steps $t/\delta t$ implemented in the experiment for $N = 2, 4, 6$ staggered sites.

N	$X_iX_j(\chi)$	$R_i(\theta,\phi)$	$Z_i(\theta)$	$t/\delta t$
2	2	0	6	39
4	9	8	16	10
6	20	12	26	4

To simulate the evolution under the Hamiltonian in Eq. (2), the product formula needs to be decomposed into the native gates in the experiment. Specifically, to implement the $Y_iY_j(\chi) = e^{-i\chi\hat{\sigma}_i^Y\hat{\sigma}_j^Y}$ (or $Z_iZ_j(\chi) = e^{-i\chi\hat{\sigma}_i^Z\hat{\sigma}_j^Z}$) gate, each qubit is rotated around the Z (or Y) axis before and after applying an $X_iX_j(\chi)$ gate. For the odd-even ordering, i.e., $\mathcal{S}_1^{\text{oe1}}$ given in Eq. (11), the circuit can be broken down into three parts: $e^{-i\delta t\hat{H}^x}$, $e^{-i\delta t\hat{H}^{ZZ}}$, and $e^{-i\delta t\hat{H}^Z}$. An example of the circuit for the Trotterized evolution with $N = 6$ is shown in Fig. 4. The number of gates needed in each Trotter step for the different values of N in the experiment are summarized in Table I. While the number of single-qubit rotations can be further reduced in the circuits, such an optimization is not considered here, since they have much lower error rates than the two-qubit gates.

The experiment starts by preparing the qubits in the vacuum state of the Hamiltonian in the limit of $x = 0$, $|\text{vac}\rangle = |\psi_0\rangle$, using $R_i(\pi, 0)$ on alternate qubits. The model parameters are set to $\mu = 0.1$ and $x = 0.6$ to ensure nontrivial

dynamics starting from the bare vacuum. We measure all the qubits in the Z basis to obtain the state populations. The state preparation and measurement errors are corrected by applying the inverse of an independently measured state-transfer matrix. The observables of interest are then calculated from the state populations using Eqs. (3)–(5).

Algorithmic and experimental errors can, in principle, produce measurement results that break the global charge conservation of the system. This means that starting from the bare-vacuum state, the probability amplitude for evolving to states with nonvanishing total charge may not be negligible. Therefore, to improve the results, one can postselect the measurements so that only outcomes in the relevant symmetry sector are kept. Since the odd-even ordering implemented in the experiment does not violate the global charge conservation, these errors result entirely from the experimental imperfections.

Figure 5(a) plots the bare-vacuum population P_{vac}, Eq. (3), and the particle-number density ν, Eq. (4), as a function of time for $N = 2$ and $\delta t = 0.5$. For $\delta t = 0.5$, the theoretical Trotterized evolution (blue dots) has no significant deviation from the exact evolution (blue line). The experimental results after postselection agree well with the theory even after 39 Trotter steps corresponding to $t = 19.5$. Postselection is shown to significantly mitigate the experimental errors for P_{vac}, especially at long evolution times. However, it does not appear as effective for the particle-number density or the survival amplitude of other initial states in general, as plotted in Appendix B. Figure 5(b) plots the local charge density Q_n, Eq. (5), derived from postselected measurement results and their deviation from the theoretical expectation for the same set of parameters. The local-charge profile is consistent with the global dynamics shown in Fig. 5(a) as the pair creation coincides with the destruction of the bare vacuum.

Figure 6 plots the same observables as a function of time for $N = 4$ and $\delta t = 0.5$. Compared with the $N = 2$ case, each Trotter step for $N = 4$ requires seven extra two-qubit gates (see Table I) and we only perform ten Trotter steps for this case. Since the experimental error dominates the Trotter error after a few Trotter steps for $\delta t = 0.5$, the Trotter step size is increased to $\delta t = 1$ in Fig. 7, doubling the simulation time. Even though the Trotter error is larger in Fig. 7 than in Fig. 6, the Trotterized evolution still qualitatively follows the exact solution. In both cases, the experimental data after postselection agree reasonably well with the numerical simulation.

Next, we increase the number of staggered sites to $N = 6$, with the results displayed in Fig. 8. Since each Trotter step now requires 20 two-qubit gates and 38 single-qubit gates, only four Trotter steps can be run before decoherence dampens the evolution. Nevertheless, the qualitative behavior, including the first revival of the bare-vacuum amplitude, can still be observed from the results.

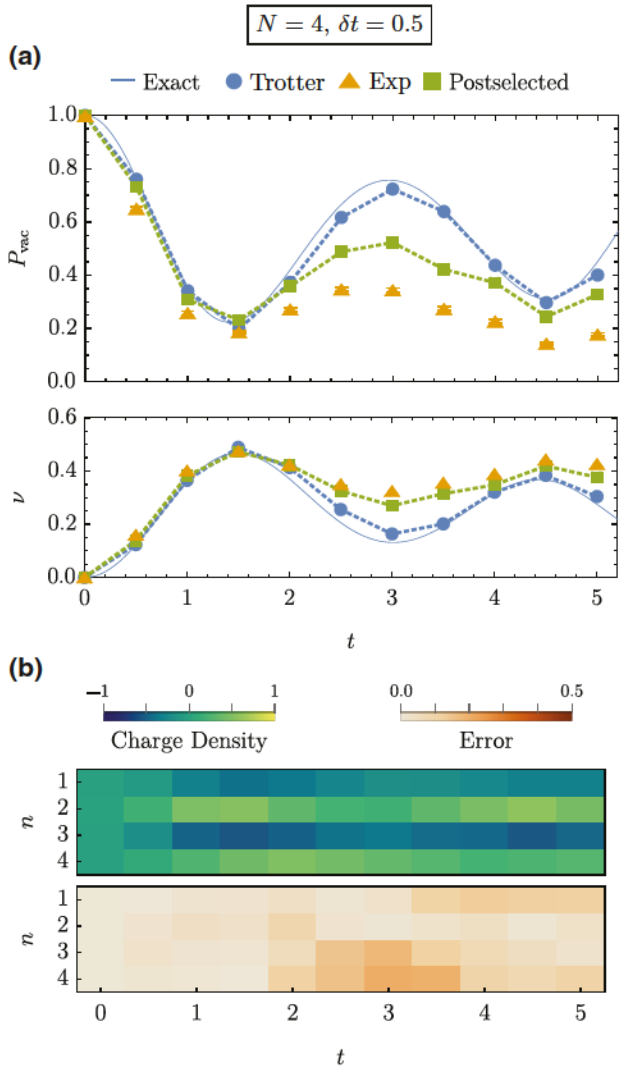

FIG. 6. Experimental results for $N = 4$ and $\delta t = 0.5$. (a) The upper plot shows fluctuation in the bare-vacuum population, $P_{\text{vac}}(t)$, while the lower plot shows the particle-number density, $\nu(t)$. (b) The upper plot shows the local charge density $Q_n(t)$ as measured in the experiment after postselection, while the lower plot shows its deviation from theory.

Finally, we study the effect of active symmetry protection by inserting rotations generated by the symmetry operator $\hat{S}_z$, as discussed in Sec. II. In the numerical study of Sec. II, a set of optimal angles is found to minimize the leakage to the symmetry-forbidden subspace caused by algorithmic error. Since such an optimal set cannot be found *a priori*, a straightforward strategy is to use a random angle at each Trotter step to average out the leakage after many Trotter steps [29]. Since the effectiveness of the scheme depends on the nature of the experimental error, it is interesting to see if symmetry protection can improve our experimental implementation.

Figure 9 plots the result of an experiment using the odd-even term ordering. As before, the initial state is the

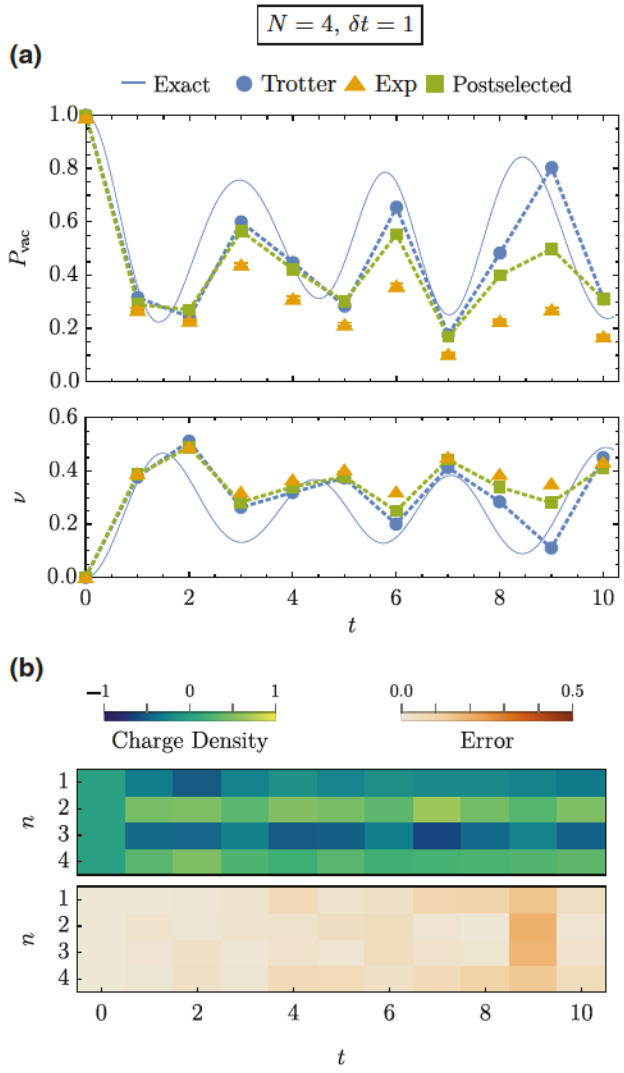

FIG. 7. Experimental results for $N = 4$ and $\delta t = 1$. (a) The upper plot shows fluctuation in the bare-vacuum population, $P_{\text{vac}}(t)$, while the lower plot shows the particle-number density, $\nu(t)$. (b) The upper plot shows the local charge density $Q_n(t)$ as measured in the experiment after postselection, while the lower plot shows its deviation from theory.

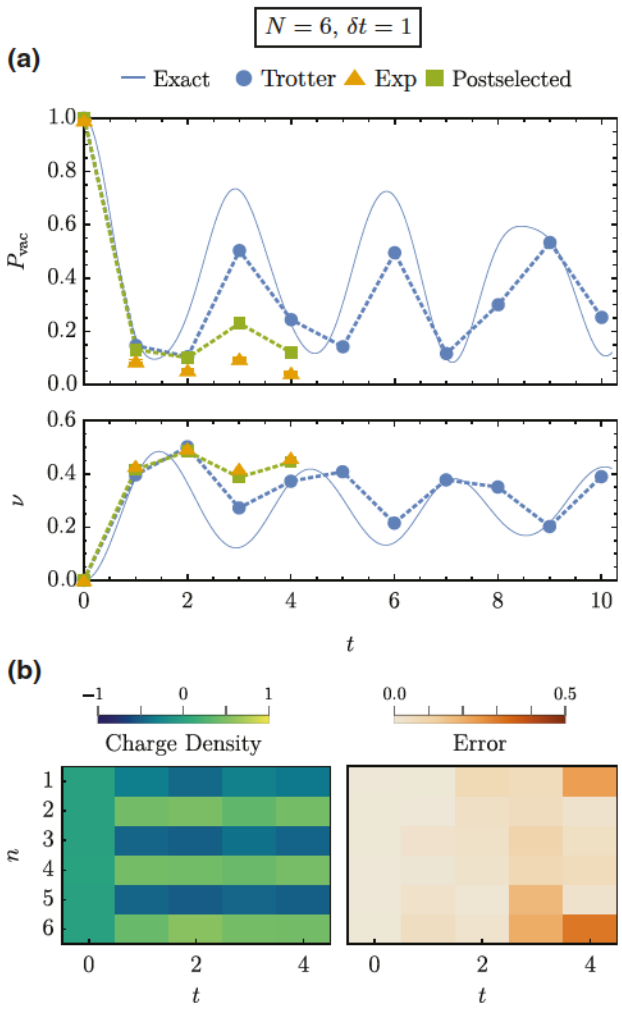

FIG. 8. Experimental results for $N = 6$ and $\delta t = 1$. (a) The upper plot shows fluctuation in the bare-vacuum population, $P_{\text{vac}}(t)$, while the lower plot shows the particle-number density, $\nu(t)$. (b) The left-hand plot shows the local charge density $Q_n(t)$ as measured in the experiment after postselection, while the right-hand plot shows its deviation from theory. At $t = 4$, we reach the gate-depth limit of the hardware.

bare vacuum. The unitaries $e^{-i\alpha_k \hat{S}_z}$, with random angles α_k given in Appendix A, are inserted between Trotter steps k and $k+1$. While the population in states forbidden by the symmetry, denoted as $P_{\overline{\text{sym}}}$ in the upper panel, decreases with symmetry protection, this reduction is not significant. Furthermore, while the deviation of the bare-vacuum population from the Trotterized theory generally decreases, postselection of symmetry-preserving measurements appears more effective in mitigating the error in this quantity than the symmetry protection as shown in the lower panel of the figure. This indicates that the experiment is dominated by noise that is not correlated in time. Note that by construction, the symmetry-protection scheme only mitigates time-correlated errors.

IV. DISCUSSION AND CONCLUSIONS

We digitally simulate the time evolution of the lattice Schwinger model with up to six qubits using the purely fermionic formulation. For a four-qubit simulation, we observe four oscillations of the particle density and the simulated time is almost four times longer than previously demonstrated using a Trotterized scheme [64, 71]. Given the long circuit depths required for dynamical gauge-theory simulations, gate fidelity, rather than qubit number, is the main limitation of our implementation. Efforts to overcome such a technical limitation are well underway [89]. To mitigate the time-correlated errors, we apply a symmetry-protection scheme [29] but find negligible effects in suppressing the errors. This

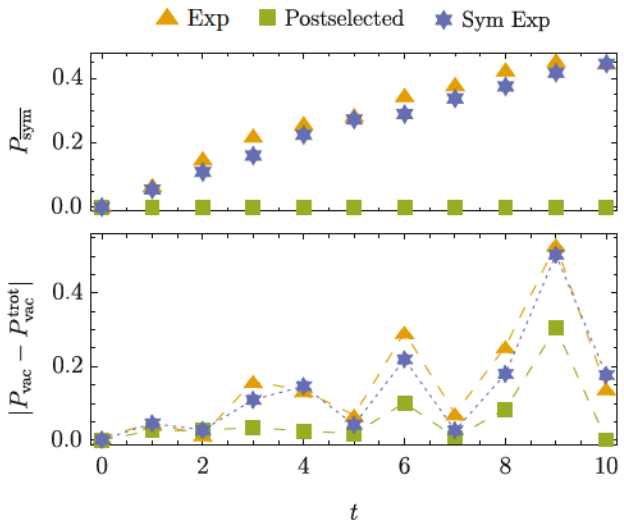

FIG. 9. The leakage to the symmetry-forbidden subspace (upper panel) and deviation of the experimental results from theory for the bare-vacuum population (lower panel) when different schemes to mitigate errors are applied: no mitigation (orange triangles), postselection (green squares), and symmetry protection (blue stars). Note that by definition, the leakage to the symmetry-forbidden subspace is zero after postselection. In both plots, $N = 4$ and $\delta t = 1.0$, the system is initiated in the bare-vacuum state and is evolved via the odd-even ordering scheme. Sym Exp refers to the experimental results with symmetry protection.

symmetry-protection investigation indicates that the dominant noise in experiment is incoherent and uncorrelated. Incoherent errors can be mitigated by postselection of the experimental measurements using symmetry considerations. Better-motivated and further-tailored schemes for mitigating incoherent errors are desired in future simulations. Furthermore, it is found that the symmetry-violating and symmetry-preserving errors can destructively contribute to given quantities and removing only one of these errors can decrease the overall accuracy. It is therefore important to also develop and apply symmetry-preserving error-suppression schemes in future experiments.

An avenue for improving the quality of the simulation is reducing the gate depth, e.g., by performing gates in parallel instead of sequentially. In our model, $e^{-i\delta t H^x}$, consisting of only nearest-neighbor interactions, can be applied in a fixed circuit depth of 4 instead of $2N$ by performing all the $X_{2i}X_{2i+1}$ terms, then all the $X_{2i+1}X_{2i+2}$ terms, in parallel. $e^{-i\delta t H^{ZZ}}$ can be reduced to depth of N instead of N^2 if non nearest-neighbor gates X_iX_{i+n}, for all i and fixed n, are performed in parallel. With trapped ions, parallel operations can be done either in multizone architectures [90,91] or in linear chains with advanced control schemes [92].

Alternatively, the gate depth can be reduced by using M-body Mølmer-Sørensen (MS) gates $\mathrm{MS}(\chi, M) \equiv e^{-i\chi \sum_{i=1}^{M} \sum_{j=i+1}^{M} \hat{\sigma}_i^X \hat{\sigma}_j^X}$ [83–85]. This approach has been implemented in Ref. [71] to reduce the number of MS operations in the simulation of the Schwinger model from $\mathcal{O}(N^2)$ to $\mathcal{O}(N)$. In general, a nontrivial optimization of both frequency and amplitude modulation of the beams may be required to implement an M-body gate with the desired rotation angles, as demonstrated in Ref. [59]. Furthermore, one should note that since an M-body MS gate has a fidelity that is roughly comparable to that of M 2-body MS (X_iX_j) gates [93], the overall fidelity of the simulation would likely be similar for both schemes.

When the fermion-boson formulation of the lattice Schwinger model is concerned, a trapped-ion-specific approach to reduce the gate count is to encode the gauge degrees of freedom into the motion of the ions as explained in Ref. [68]. Besides the standard set of gates, the proposed hybrid digital-analog scheme involves both spin-phonon and phonon-phonon gates. This approach leads to a reduction in both the number of qubits and the number of entangling gates compared with a fully digital algorithm involving the gauge bosons [22]. Future experimental implementations will determine the realistic fidelity of the operations involving dynamical phonons.

To make implementations of more complex gauge theories possible, including non-Abelian and higher-dimensional models, unifying physics insights, algorithm optimization, hardware implementation, and postprocessing is required, as demonstrated in this work. In this context, it would be interesting to investigate whether more resource-efficient encodings of such theories exist, if optimal Trotter decompositions and term ordering schemes can be found, to what degree these preserve local gauge symmetries, whether information regarding the initial state and the symmetries can be incorporated to further tighten the algorithmic error bounds [70,94–99], how to balance these errors with experimental errors, and whether symmetry-protection schemes are advantageous in suppressing algorithmic and experimental errors. While progress along these lines is already being made [23,24,27,30,32,36,67,100–108], further technological advances in quantum hardware are essential to enable advanced gauge-theory simulations in the upcoming years.

ACKNOWLEDGMENTS

We acknowledge Andrew Shaw's involvement at early stages of this work. We are grateful to Guido Pagano for valuable discussions. Z.D. is supported in part by the U.S. Department of Energy (DOE) Office of Science Early Career Award, under Award No. DE-SC0020271, and by the Maryland Center for Fundamental Physics. Z.D. further acknowledges the RIKEN Center for Accelerator-Based Sciences, Wako, Japan for their support during earlier stages of this work. Z.D. and N.M.L. acknowledge support by the DOE Office of Science, Office of Nuclear Physics, under Award No. DE-SC0021143.

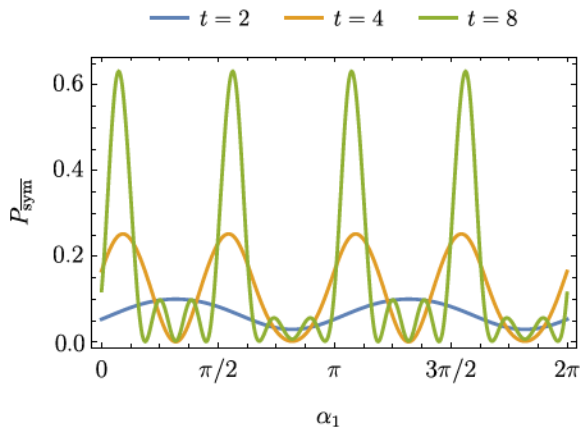

FIG. 10. The population of the symmetry-forbidden subspace as a function of the angles α_1 for $t = 2, 4, 8$, for $\mu = 0.1, x = 0.6$, $N = 4$, and $\delta t = 1$. We choose α_1 to be the smallest angle that minimizes $P_{\overline{\text{sym}}}$ at each t.

N.M.L. received support from the National Science Foundation Quantum Leap Challenge Institutes (QLCI) (Grant No. OMA-2120757) and Physics Frontiers Centers (PFC) (Grant No. PHY-1430094). N.M.L. acknowledges funding from the U.S. Army Research Laboratory (ARL) Maryland-ARL Quantum Partnership (MAQP), under Grant No. W911NF-19-2-0181. A.M.G. is supported by a Joint Quantum Institute Postdoctoral Fellowship. M.C.T. acknowledges the Nippon Telegraph and Telephone (NTT) Research Quantum Algorithms and Machine Learning Grant No. AGMT DTD 9/24/20.

APPENDIX A: OPTIMAL AND RANDOM ANGLES FOR SYMMETRY PROTECTION

In Fig. 3, we study how well the symmetry-protected time evolution given in Eq. (16) suppresses the symmetry-breaking Trotter errors for a simulation with the XYZ ordering with $\mu = 0.1$, $x = 0.6$, $N = 4$, and $\delta t = 1$. As mentioned in Sec. II C, for the time evolution with a particular t, the angle of rotation, α_k, for the kth Trotter step depends on α_1 in the first Trotter step as $\alpha_k = k\alpha_1$, where $0 \le \alpha_1 < 2\pi$. We choose α_1 to be the smallest angle with which the leakage to the symmetry-broken subspace at time t is minimized.

Figure 10 displays a few examples of how the leakage varies as a function of α_1 for selected times t. As shown in the plot, there are several values of α_1 that minimize the leakage and the number of minima tends to increase with increasing t. The optimal value of α_1 is determined from the smallest minimum found at each t. These values are listed in Table II.

TABLE II. The values of α_1 used for the symmetry-protected XYZ ordering in Fig. 3 at different times t, together with the corresponding leakage to the symmetry-forbidden subspace.

t	α_1	$P_{\overline{\text{sym}}}$
1	0	0.0346
2	0.8184π	0.0294
3	0.8184π	0.0260
4	0.3183π	0.0006
5	0.8811π	0.0128
6	0.2314π	0.0018
7	0.4370π	0.0201
8	0.1875π	0.0011
9	0.8496π	0.0055
10	0.9887π	0.0000

Meanwhile, the angles α_k for the symmetry-protected evolution in the experiment in Fig. 9 are chosen at random from a uniform distribution in the interval $[0, 2\pi]$. These angles are listed in Table III.

APPENDIX B: STATE POPULATIONS

The population in the bare vacuum as a function of time is displayed in Fig. 7 of the main text. For completeness, we also plot in Fig. 11 the population of all allowed states as a function of time for the case of $N = 4$ and $\delta t = 1.0$.

TABLE III. The randomly chosen values of α_k used in the experiment to study the effect of symmetry protection on experimental error. The result is presented in Fig. 9.

t	α_1	α_2	α_3	α_4	α_5	α_6	α_7	α_8	α_9	α_{10}
1	0.9559π	—	—	—	—	—	—	—	—	—
2	1.1461π	0.2987π	—	—	—	—	—	—	—	—
3	0.0150π	0.6927π	1.6279π	—	—	—	—	—	—	—
4	0.5861π	0.0333π	0.0787π	0.1613π	—	—	—	—	—	—
5	1.7496π	1.7986π	0.4505π	1.4374π	0.3222π	—	—	—	—	—
6	1.7205π	0.0706π	1.0666π	1.5912π	1.0554π	0.8444π	—	—	—	—
7	0.2499π	0.2990π	0.1212π	0.6793π	0.9988π	0.9218π	1.8565π	—	—	—
8	1.7974π	0.7531π	0.0548π	0.4236π	1.8081π	1.7279π	0.4253π	0.8807π	—	—
9	0.8880π	0.3908π	1.7202π	1.7779π	1.1028π	1.7425π	1.6552π	0.0604π	0.2346π	—
10	0.7112π	1.1025π	1.3913π	0.5387π	1.7179π	1.0585π	0.2870π	0.8636π	1.6639π	1.5434π

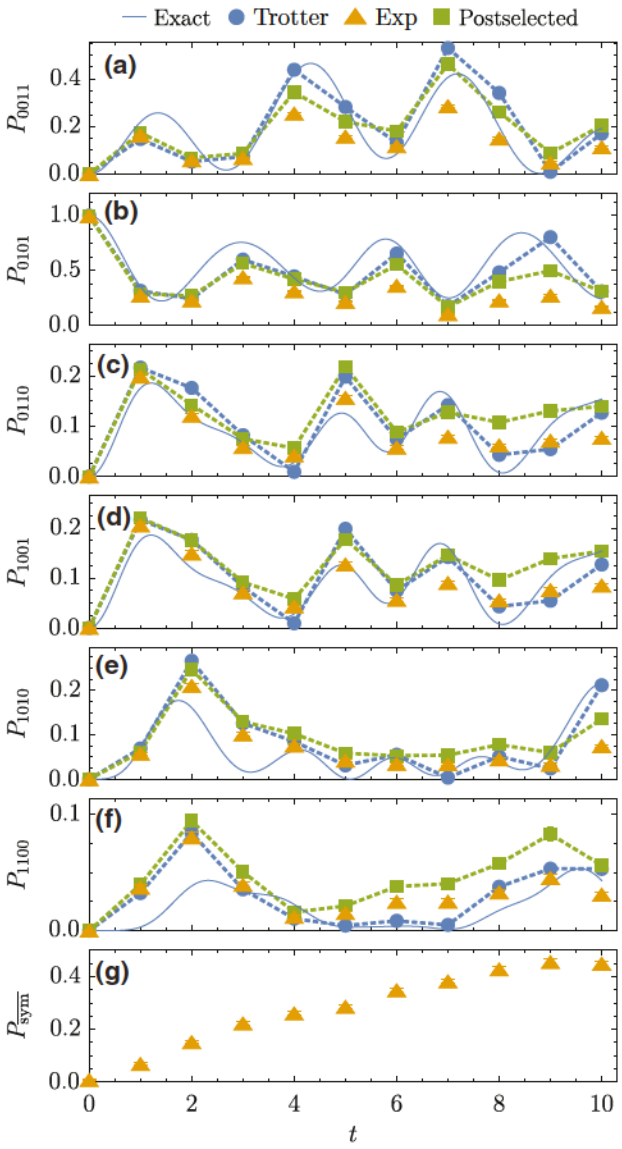

FIG. 11. The evolution of states characterized by the quantity $P_\Psi \equiv |\langle\Psi|e^{-itH}|\psi_0\rangle|^2$ in the (a)–(f) symmetry-allowed and (g) symmetry-forbidden subspace for $N = 4$ and $\delta t = 1.0$, starting from the bare-vacuum state $|\psi_0\rangle$. Note that $P_{0101} \equiv P_{\text{vac}}$, which is also plotted in Fig. 7 of the main text. The effectiveness of post-selection in mitigating errors is both quantity and time dependent and, in some cases, it ceases to improve the agreement with theory at larger times.

Additionally, the cumulative population in the symmetry-forbidden sector, $P_{\overline{\text{sym}}}$, is shown, demonstrating the rate at which the leakage to the symmetry-forbidden sector grows.

[1] R. P. Feynman, Simulating physics with computers, Int. J. Theor. Phys. **21**, 467 (1982).

[2] S. Lloyd, Universal quantum simulators, Science **273**, 1073 (1996).

[3] A. M. Childs, Y. Su, M. C. Tran, N. Wiebe, and S. Zhu, Theory of Trotter Error with Commutator Scaling, Phys. Rev. X **11**, 011020 (2021).

[4] A. M. Childs and N. Wiebe, Hamiltonian simulation using linear combinations of unitary operations, Quantum Inf. Comput. **12**, 901 (2012).

[5] D. W. Berry, A. M. Childs, R. Cleve, R. Kothari, and R. D. Somma, Simulating Hamiltonian Dynamics with a Truncated Taylor Series, Phys. Rev. Lett. **114**, 090502 (2015).

[6] G. H. Low and I. L. Chuang, Optimal Hamiltonian Simulation by Quantum Signal Processing, Phys. Rev. Lett. **118**, 010501 (2017).

[7] G. H. Low and I. L. Chuang, Hamiltonian simulation by qubitization, Quantum **3**, 163 (2019).

[8] S. Chakraborty, A. Gilyén, and S. Jeffery, in *46th International Colloquium on Automata, Languages, and Programming (ICALP 2019)*, Leibniz International Proceedings in Informatics (LIPIcs), Vol. 132, edited by C. Baier, I. Chatzigiannakis, P. Flocchini, and S. Leonardi (Schloss Dagstuhl–Leibniz-Zentrum für Informatik, Dagstuhl, Germany, 2019), p. 33:1.

[9] A. Gilyén, Y. Su, G. H. Low, and N. Wiebe, in *Proceedings of the 51st Annual ACM SIGACT Symposium on Theory of Computing* (2019), p. 193.

[10] A. Kalev and I. Hen, Quantum algorithm for simulating Hamiltonian dynamics with an off-diagonal series expansion, Quantum **5**, 426 (2021).

[11] A. M. Childs and Y. Su, Nearly Optimal Lattice Simulation by Product Formulas, Phys. Rev. Lett. **123**, 050503 (2019).

[12] T. F. Stetina, A. Ciavarella, X. Li, and N. Wiebe, Simulating effective QED on quantum computers, Quantum **6**, 622 (2022).

[13] J. Lee, D. W. Berry, C. Gidney, W. J. Huggins, J. R. McClean, N. Wiebe, and R. Babbush, Even more efficient quantum computations of chemistry through tensor hypercontraction, PRX Quantum **2**, 030305 (2021).

[14] V. von Burg, G. H. Low, T. Häner, D. S. Steiger, M. Reiher, M. Roetteler, and M. Troyer, Quantum computing enhanced computational catalysis, Phys. Rev. Res. **3**, 033055 (2021).

[15] W. J. Huggins, J. R. McClean, N. C. Rubin, Z. Jiang, N. Wiebe, K. B. Whaley, and R. Babbush, Efficient and noise resilient measurements for quantum chemistry on near-term quantum computers, Npj Quantum Inf. **7**, 23 (2021).

[16] R. Babbush, C. Gidney, D. W. Berry, N. Wiebe, J. McClean, A. Paler, A. Fowler, and H. Neven, Encoding Electronic Spectra in Quantum Circuits with Linear t Complexity, Phys. Rev. X **8**, 041015 (2018).

[17] R. Babbush, N. Wiebe, J. McClean, J. McClain, H. Neven, and G. K.-L. Chan, Low-Depth Quantum Simulation of Materials, Phys. Rev. X **8**, 011044 (2018).

[18] S. P. Jordan, K. S. Lee, and J. Preskill, Quantum algorithms for quantum field theories, Science **336**, 1130 (2012).

[19] N. Klco and M. J. Savage, Digitization of scalar fields for quantum computing, Phys. Rev. A **99**, 052335 (2019).

[20] J. Barata, N. Mueller, A. Tarasov, and R. Venugopalan, Single-particle digitization strategy for quantum computation of a ϕ^4 scalar field theory, Phys. Rev. A **103**, 042410 (2021).
[21] H. Lamm, S. Lawrence, and Y. Yamauchi, (NuQS), General methods for digital quantum simulation of gauge theories, Phys. Rev. D **100**, 034518 (2019).
[22] A. F. Shaw, P. Lougovski, J. R. Stryker, and N. Wiebe, Quantum algorithms for simulating the lattice Schwinger model, Quantum **4**, 306 (2020).
[23] A. Ciavarella, N. Klco, and M. J. Savage, Trailhead for quantum simulation of SU(3) Yang-Mills lattice gauge theory in the local multiplet basis, Phys. Rev. D **103**, 094501 (2021).
[24] A. Kan and Y. Nam, Lattice quantum chromodynamics and electrodynamics on a universal quantum computer, arXiv:2107.12769 (2021).
[25] M. Kreshchuk, W. M. Kirby, G. Goldstein, H. Beauchemin, and P. J. Love, Quantum simulation of quantum field theory in the light-front formulation, Phys. Rev. A **105**, 032418 (2022).
[26] J. Liu and Y. Xin, Quantum simulation of quantum field theories as quantum chemistry, J. High Energy Phys. **2020**, 11 (2020).
[27] D. Paulson, L. Dellantonio, J. F. Haase, A. Celi, A. Kan, A. Jena, C. Kokail, R. van Bijnen, K. Jansen, P. Zoller, and C. A. Muschik, Simulating 2D effects in lattice gauge theories on a quantum computer, PRX Quantum **2**, 030334 (2021).
[28] B. Nachman, D. Provasoli, W. A. de Jong, and C. W. Bauer, Quantum Algorithm for High Energy Physics Simulations, Phys. Rev. Lett. **126**, 062001 (2021).
[29] M. C. Tran, Y. Su, D. Carney, and J. M. Taylor, Faster digital quantum simulation by symmetry protection, PRX Quantum **2**, 010323 (2021).
[30] H. Lamm, S. Lawrence, and Y. Yamauchi, (NuQS), Suppressing Coherent Gauge Drift in Quantum Simulations, arXiV:2005.12688 (2020).
[31] J. C. Halimeh, H. Lang, J. Mildenberger, Z. Jiang, and P. Hauke, Gauge-symmetry protection using single-body terms, PRX Quantum **2**, 040311 (2021).
[32] J. C. Halimeh, H. Lang, and P. Hauke, Gauge protection in non-Abelian lattice gauge theories, New J. Phys. **24**, 033015 (2022).
[33] K. Stannigel, P. Hauke, D. Marcos, M. Hafezi, S. Diehl, M. Dalmonte, and P. Zoller, Constrained Dynamics via the Zeno Effect in Quantum Simulation: Implementing non-Abelian Lattice Gauge Theories with Cold Atoms, Phys. Rev. Lett. **112**, 120406 (2014).
[34] V. Kasper, T. V. Zache, F. Jendrzejewski, M. Lewenstein, and E. Zohar, Non-Abelian gauge invariance from dynamical decoupling, arXiv:2012.08620 (2020).
[35] J. R. Stryker, Oracles for Gauss's law on digital quantum computers, Phys. Rev. A **99**, 042301 (2019).
[36] I. Raychowdhury and J. R. Stryker, Solving Gauss's law on digital quantum computers with loop-string-hadron digitization, Phys. Rev. Res. **2**, 033039 (2020).
[37] A. Kandala, K. Temme, A. D. Córcoles, A. Mezzacapo, J. M. Chow, and J. M. Gambetta, Error mitigation extends the computational reach of a noisy quantum processor, Nature **567**, 491 (2019).
[38] K. Temme, S. Bravyi, and J. M. Gambetta, Error Mitigation for Short-Depth Quantum Circuits, Phys. Rev. Lett. **119**, 180509 (2017).
[39] S. Endo, S. C. Benjamin, and Y. Li, Practical Quantum Error Mitigation for Near-Future Applications, Phys. Rev. X **8**, 031027 (2018).
[40] S. S. Tannu and M. K. Qureshi, in *Proceedings of the 52nd Annual IEEE/ACM International Symposium on Microarchitecture*, MICRO '52 (Association for Computing Machinery, New York, 2019), p. 279.
[41] J. J. Wallman and J. Emerson, Noise tailoring for scalable quantum computation via randomized compiling, Phys. Rev. A **94**, 052325 (2016).
[42] A. Shaw, Classical-Quantum Noise Mitigation for NISQ Hardware, arXiv:2105.08701 (2021).
[43] A. He, B. Nachman, W. A. de Jong, and C. W. Bauer, Zero-noise extrapolation for quantum-gate error mitigation with identity insertions, Phys. Rev. A **102**, 012426 (2020).
[44] P. Czarnik, A. Arrasmith, P. J. Coles, and L. Cincio, Error mitigation with Clifford quantum-circuit data, Quantum **5**, 592 (2021).
[45] J. Vovrosh, K. E. Khosla, S. Greenaway, C. Self, M. S. Kim, and J. Knolle, Simple mitigation of global depolarizing errors in quantum simulations, Phys. Rev. E **104**, 035309 (2021).
[46] Y. Aoki *et al.*, FLAG Review 2021, arXiv:2111.09849 (2021).
[47] S. R. Beane, W. Detmold, K. Orginos, and M. J. Savage, Nuclear physics from lattice QCD, Prog. Part. Nucl. Phys. **66**, 1 (2011).
[48] H.-T. Ding, F. Karsch, and S. Mukherjee, Thermodynamics of strong-interaction matter from lattice QCD, Int. J. Mod. Phys. E **24**, 1530007 (2015).
[49] R. A. Briceno, J. J. Dudek, and R. D. Young, Scattering processes and resonances from lattice QCD, Rev. Mod. Phys. **90**, 025001 (2018).
[50] C. Ratti, Lattice QCD and heavy ion collisions: A review of recent progress, Rep. Prog. Phys. **81**, 084301 (2018).
[51] Z. Davoudi, W. Detmold, K. Orginos, A. Parreño, M. J. Savage, P. Shanahan, and M. L. Wagman, Nuclear matrix elements from lattice QCD for electroweak and beyond-standard-model processes, Phys. Rep. **900**, 1 (2021).
[52] E. A. Calzetta and B.-L. B. Hu, *Nonequilibrium Quantum Field Theory*, Cambridge Monographs on Mathematical Physics (Cambridge University Press, 2008).
[53] J. Schwinger, On gauge invariance and vacuum polarization, Phys. Rev. **82**, 664 (1951).
[54] J. Schwinger, Gauge invariance and mass. II, Phys. Rev. **128**, 2425 (1962).
[55] J. Schwinger, The theory of quantized fields. II, Phys. Rev. **91**, 713 (1953).
[56] D. Banerjee, M. Dalmonte, M. Müller, E. Rico, P. Stebler, U.-J. Wiese, and P. Zoller, Atomic Quantum Simulation of Dynamical Gauge Fields Coupled to Fermionic Matter: From String Breaking to Evolution after a Quench, Phys. Rev. Lett. **109**, 175302 (2012).
[57] E. Zohar, J. I. Cirac, and B. Reznik, Quantum simulations of lattice gauge theories using ultracold atoms in optical lattices, Rep. Prog. Phys. **79**, 014401 (2015).
[58] D. Yang, G. S. Giri, M. Johanning, C. Wunderlich, P. Zoller, and P. Hauke, Analog quantum simulation of (1 +

1)-dimensional lattice QED with trapped ions, Phys. Rev. A **94**, 052321 (2016).
[59] Z. Davoudi, M. Hafezi, C. Monroe, G. Pagano, A. Seif, and A. Shaw, Towards analog quantum simulations of lattice gauge theories with trapped ions, Phys. Rev. Res. **2**, 023015 (2020).
[60] F. M. Surace, P. P. Mazza, G. Giudici, A. Lerose, A. Gambassi, and M. Dalmonte, Lattice Gauge Theories and String Dynamics in Rydberg Atom Quantum Simulators, Phys. Rev. X **10**, 021041 (2020).
[61] D. Luo, J. Shen, M. Highman, B. K. Clark, B. DeMarco, A. X. El-Khadra, and B. Gadway, Framework for simulating gauge theories with dipolar spin systems, Phys. Rev. A **102**, 032617 (2020).
[62] B. Andrade, Z. Davoudi, T. Graß, M. Hafezi, G. Pagano, and A. Seif, Engineering an effective three-spin Hamiltonian in trapped-ion systems for applications in quantum simulation, Quantum Sci. Technol. **7**, 034001 (2022).
[63] C. Muschik, M. Heyl, E. Martinez, T. Monz, P. Schindler, B. Vogell, M. Dalmonte, P. Hauke, R. Blatt, and P. Zoller, U(1) Wilson lattice gauge theories in digital quantum simulators, New J. Phys. **19**, 103020 (2017).
[64] N. Klco, E. F. Dumitrescu, A. J. McCaskey, T. D. Morris, R. C. Pooser, M. Sanz, E. Solano, P. Lougovski, and M. J. Savage, Quantum-classical computation of Schwinger model dynamics using quantum computers, Phys. Rev. A **98**, 032331 (2018).
[65] H.-H. Lu, N. Klco, J. M. Lukens, T. D. Morris, A. Bansal, A. Ekström, G. Hagen, T. Papenbrock, A. M. Weiner, M. J. Savage, and P. Lougovski, Simulations of subatomic many-body physics on a quantum frequency processor, Phys. Rev. A **100**, 012320 (2019).
[66] B. Chakraborty, M. Honda, T. Izubuchi, Y. Kikuchi, and A. Tomiya, Digital Quantum Simulation of the Schwinger Model with Topological Term via Adiabatic State Preparation, arXiv:2001.00485 (2020).
[67] J. R. Stryker, Shearing approach to gauge invariant Trotterization, arXiv:2105.11548 (2021).
[68] Z. Davoudi, N. M. Linke, and G. Pagano, Toward simulating quantum field theories with controlled phonon-ion dynamics: A hybrid analog-digital approach, Phys. Rev. Res. **3**, 043072 (2021).
[69] G. Pederiva, A. Bazavov, B. Henke, L. Hostetler, D. Lee, H.-W. Lin, and A. Shindler, in *38th International Symposium on Lattice Field Theory* (2021).
[70] A. Rajput, A. Roggero, and N. Wiebe, Hybridized Methods for Quantum Simulation in the Interaction Picture, arXiv:2109.03308 (2021).
[71] E. A. Martinez, C. A. Muschik, P. Schindler, D. Nigg, A. Erhard, M. Heyl, P. Hauke, M. Dalmonte, T. Monz, P. Zoller, and R. Blatt, Real-time dynamics of lattice gauge theories with a few-qubit quantum computer, Nature **534**, 516 (2016).
[72] C. Kokail, C. Maier, R. van Bijnen, T. Brydges, M. K. Joshi, P. Jurcevic, C. A. Muschik, P. Silvi, R. Blatt, C. F. Roos, and P. Zoller, Self-verifying variational quantum simulation of lattice models, Nature **569**, 355 (2019).
[73] H. Bernien, S. Schwartz, A. Keesling, H. Levine, A. Omran, H. Pichler, S. Choi, A. S. Zibrov, M. Endres, M. Greiner, V. Vuletić, and M. D. Lukin, Probing many-body dynamics on a 51-atom quantum simulator, Nature **551**, 579 (2017).
[74] A. Mil, T. V. Zache, A. Hegde, A. Xia, R. P. Bhatt, M. K. Oberthaler, P. Hauke, J. Berges, and F. Jendrzejewski, A scalable realization of local U(1) gauge invariance in cold atomic mixtures, Science **367**, 1128 (2020).
[75] Z.-Y. Zhou, G.-X. Su, J. C. Halimeh, R. Ott, H. Sun, P. Hauke, B. Yang, Z.-S. Yuan, J. Berges, and J.-W. Pan, Thermalization dynamics of a gauge theory on a quantum simulator, arXiv:2107.13563 (2021).
[76] W. A. de Jong, K. Lee, J. Mulligan, M. Płoskoń, F. Ringer, and X. Yao, Quantum simulation of non-equilibrium dynamics and thermalization in the Schwinger model, arXiv:2106.08394 (2021).
[77] J. Kogut and L. Susskind, Hamiltonian formulation of Wilson's lattice gauge theories, Phys. Rev. D **11**, 395 (1975).
[78] C. J. Hamer, Z. Weihong, and J. Oitmaa, Series expansions for the massive Schwinger model in Hamiltonian lattice theory, Phys. Rev. D **56**, 55 (1997).
[79] M. Suzuki, General theory of fractal path integrals with applications to many-body theories and statistical physics, J. Math. Phys. **32**, 400 (1991).
[80] We group the interactions in $\hat{H}^{ZZ}$ and $\hat{H}^{Z}$ into the kth term in the estimation of the Trotter error in Eq. (10). Since the terms in $\hat{H}^{ZZ}$ and $\hat{H}^{Z}$ commute, further Trotterizing the evolution under $\hat{H}^{ZZ}$ and $\hat{H}^{Z}$ into one- and two-qubit gates introduces no additional Trotter error.
[81] S. Olmschenk, K. C. Younge, D. L. Moehring, D. N. Matsukevich, P. Maunz, and C. Monroe, Manipulation and detection of a trapped Yb^{+} hyperfine qubit, Phys. Rev. A **76**, 052314 (2007).
[82] S. Debnath, N. M. Linke, C. Figgatt, K. A. Landsman, K. Wright, and C. Monroe, Demonstration of a small programmable quantum computer with atomic qubits, Nature **536**, 63 (2016).
[83] A. Sorensen and K. Molmer, Quantum Computation with Ions in Thermal Motion, Phys. Rev. Lett. **82**, 1971 (1999).
[84] G. J. Milburn, S. Schneider, and D. F. V. James, Ion trap quantum computing with warm ions, Fortschritte der Physik **48**, 801 (2000).
[85] E. Solano, R. L. de Matos Filho, and N. Zagury, Deterministic Bell states and measurement of the motional state of two trapped ions, Phys. Rev. A **59**, R2539 (1999).
[86] T. Choi, S. Debnath, T. A. Manning, C. Figgatt, Z.-X. Gong, L.-M. Duan, and C. Monroe, Optimal Quantum Control of Multimode Couplings between Trapped Ion Qubits for Scalable Entanglement, Phys. Rev. Lett. **112**, 190502 (2014).
[87] K. A. Landsman, C. Figgatt, T. Schuster, N. M. Linke, B. Yoshida, N. Y. Yao, and C. Monroe, Verified quantum information scrambling, Nature **567**, 61 (2019).
[88] D. Zhu, Z.-P. Cian, C. Noel, A. Risinger, D. Biswas, L. Egan, Y. Zhu, A. M. Green, C. H. Alderete, N. H. Nguyen, Q. Wang, A. Maksymov, Y. Nam, M. Cetina, N. M. Linke, M. Hafezi, and C. Monroe, Cross-Platform Comparison of Arbitrary Quantum Computations, arXiv:2107.11387 (2021).
[89] L. Egan, D. M. Debroy, C. Noel, A. Risinger, D. Zhu, D. Biswas, M. Newman, M. Li, K. R. Brown, M. Cetina, and

C. Monroe, Fault-tolerant control of an error-corrected qubit, Nature **598**, 281 (2021).

[90] D. Kielpinski, C. Monroe, and D. J. Wineland, Architecture for a large-scale ion-trap quantum computer, Nature **417**, 709 (2002).

[91] C. Ryan-Anderson, J. G. Bohnet, K. Lee, D. Gresh, A. Hankin, J. P. Gaebler, D. Francois, A. Chernoguzov, D. Lucchetti, N. C. Brown, T. M. Gatterman, S. K. Halit, K. Gilmore, J. Gerber, B. Neyenhuis, D. Hayes, and R. P. Stutz, Realization of Real-Time Fault-Tolerant Quantum Error Correction, Phys. Rev. X **11**, 041058 (2021).

[92] C. Figgatt, A. Ostrander, N. M. Linke, K. A. Landsman, D. Zhu, D. Maslov, and C. Monroe, Parallel entangling operations on a universal ion-trap quantum computer, Nature **572**, 368 (2019).

[93] T. Monz, P. Schindler, J. T. Barreiro, M. Chwalla, D. Nigg, W. A. Coish, M. Harlander, W. Hänsel, M. Hennrich, and R. Blatt, 14-Qubit Entanglement: Creation and Coherence, Phys. Rev. Lett. **106**, 130506 (2011).

[94] Y. Su, H.-Y. Huang, and E. T. Campbell, Nearly tight Trotterization of interacting electrons, Quantum **5**, 495 (2021).

[95] D. An, D. Fang, and L. Lin, Time-dependent unbounded Hamiltonian simulation with vector norm scaling, Quantum **5**, 459 (2021).

[96] C. Yi and E. Crosson, Spectral analysis of product formulas for quantum simulation, npj Quantum Inf **8**, 37 (2022).

[97] Q. Zhao, Y. Zhou, A. F. Shaw, T. Li, and A. M. Childs, Hamiltonian simulation with random inputs, arXiv:2111.04773 (2021).

[98] B. Şahinoğlu and R. D. Somma, Hamiltonian simulation in the low-energy subspace, Npj Quantum Inf. **7**, 119 (2021).

[99] Y. Tong, V. V. Albert, J. R. McClean, J. Preskill, and Y. Su, Provably accurate simulation of gauge theories and bosonic systems, arXiv:2110.06942 (2021).

[100] N. Klco, M. J. Savage, and J. R. Stryker, SU(2) non-Abelian gauge field theory in one dimension on digital quantum computers, Phys. Rev. D **101**, 074512 (2020).

[101] Y. Y. Atas, J. Zhang, R. Lewis, A. Jahanpour, J. F. Haase, and C. A. Muschik, SU(2) hadrons on a quantum computer via a variational approach, Nat. Commun. **12**, 6499 (2021).

[102] S. A Rahman, R. Lewis, E. Mendicelli, and S. Powell, SU(2) lattice gauge theory on a quantum annealer, Phys. Rev. D **104**, 034501 (2021).

[103] J. F. Haase, L. Dellantonio, A. Celi, D. Paulson, A. Kan, K. Jansen, and C. A. Muschik, A resource efficient approach for quantum and classical simulations of gauge theories in particle physics, Quantum **5**, 393 (2021).

[104] I. Raychowdhury and J. R. Stryker, Loop, string, and hadron dynamics in SU(2) Hamiltonian lattice gauge theories, Phys. Rev. D **101**, 114502 (2020).

[105] Z. Davoudi, I. Raychowdhury, and A. Shaw, Search for efficient formulations for Hamiltonian simulation of non-Abelian lattice gauge theories, Phys. Rev. D **104**, 074505 (2021).

[106] M. S. Alam, S. Hadfield, H. Lamm, and A. C. Y. Li, Quantum Simulation of Dihedral Gauge Theories, arXiv:2108.13305 (2021).

[107] A. N. Ciavarella and I. A. Chernyshev, Preparation of the SU(3) Lattice Yang-Mills Vacuum with Variational Quantum Methods, arXiv:2112.09083 (2021).

[108] N. Klco, A. Roggero, and M. J. Savage, Standard Model Physics and the Digital Quantum Revolution: Thoughts about the Interface, Rep. Prog. Phys. (2022).